



Lattice distortion induced electronic coupling results in exceptional enhancement in the activity of bimetallic PtMn nanocatalysts



Xin Jin ^{a,b}, Chun Zeng ^a, Wenjuan Yan ^{a,b}, Meng Zhao ^a, Pallavi Bobba ^a, Honghong Shi ^a, Prem S. Thapa ^c, Bala Subramaniam ^a, Raghunath V. Chaudhari ^{a,*}

^a Center for Environmentally Beneficial Catalysis, Department of Chemical and Petroleum Engineering, 1501 Wakarusa Drive, University of Kansas, Lawrence, KS 66047, USA

^b State Key Laboratory for Heavy Oil Processing, College of Chemical Engineering, China University of Petroleum, Qingdao 266580, China

^c Microscopy and Analytical Imaging Laboratory, Haworth Hall, 1200 Sunnyside Ave, University of Kansas, Lawrence, KS 66045, USA

ARTICLE INFO

Article history:

Received 23 November 2016

Received in revised form 23 January 2017

Accepted 26 January 2017

Available online 28 January 2017

Keywords:

Lattice mismatch

Distortion

Anisotropic growth

Bimetallic cluster

Oxidation reaction

ABSTRACT

Lattice strain plays a critical role in structural heterogeneity and surface electronic properties of bimetallic nanocatalysts. However, understanding of how to engineer optimal electron transfer in anisotropic bimetallic crystals remains a grand challenge to achieve enhanced catalytic performances. We investigate beyond conventional polymer based core-shell and alloy structures, and present unique lattice distorted PtMn catalysts fabricated via a cooperative self-assembly method. The strong internal strain between Pt and Mn lattices is found to induce the structural distortion of anisotropic PtMn crystals and formation of asymmetric flower shapes, leading to stretched Pt and contracted Mn lattices. Such distorted bimetallic crystals exhibit unusual electronic coupling and an eight-fold synergistic enhancement in catalytic oxidation of renewable biomass feedstocks compared with monometallic Pt catalysts. The novel synthesis technique and revealed electronic coupling mechanism described herein opens the door for the rational discovery of other bimetallic nanocatalysts with positive synergy.

© 2017 Published by Elsevier B.V.

1. Introduction

The development of novel catalytic materials is a key for resource-efficient technologies for platform chemicals with reduced environmental impact [1–3]. Extensive research has already shown that bimetallic and multimetallic catalysts often exhibit enhanced catalytic performances compared with monometallic ones due to tunable morphology and composition [4,5]. Although these materials can be synthesized with precise control and particle size and tailored structures such as cubic, rhombic and octahedral shapes, they often consist of low indexed facets with limited surface catalytic activities [6–8]. Therefore, the discovery of novel nanomaterials with enhanced anisotropy and tunable electron configuration, which display high surface catalytic activities, has received much attention in recent years [9]. In the area of bimetallic materials, Pt-based nanostructured catalysts have been one of the most extensively studied systems because they not only show exceptional performances in fuel cell and petro-

chemical upgrading, but also in emerging areas such as biomass conversion and solar cells [10].

In the past decade, major research efforts have been made on fabricating bimetallic Pt-3d metal nanomaterials due to their tunable synergy in catalysis [6,11–15]. It is established in classic catalysis theories that atoms on highly indexed sites display superior activities than others. Therefore, conventional strategies on tuning the surface geometries of bimetallic crystals, and thereby to enhance catalytic activity, is by altering the morphologies of Pt-3d bimetallic structures through adding ligands [16]. Manipulation of crystal growth kinetics using ligand-metal interaction as the external driving force results in enlargement of surface roughness. This well-known methodology has been established by several research groups and summarized in several reviews [4–10,16,17]. Numerous results have confirmed that PtCo, PtCu, PtNi and PtFe particles with cubic, spherical, truncated octahedral and wired structures can be fabricated by mixing ligands [e.g. polyvinylpyrrolidone (PVP)] with metal precursors, in solvents containing polyols or amines [18–21]. For example, a two-step method involving PVP mixed with Cu seeds led to hollow nanocaged or nanoframe structured PtCu particles [22]. Branched PtNi nanostructures are reported using Pt seeds as templates [23,24], while didodecyldimethylammonium bromide stabilized Ni seeds generate PtNi nanodendrites [25].

* Corresponding author.

E-mail address: rvc1948@ku.edu (R.V. Chaudhari).

Similar techniques have also been employed to synthesize other 3d metal based nanomaterials [26–32], as well as other bimetallic combination such as PtAu, PtPd, etc. [10]. It is clear that two-step ligand directed seed/template growth is the main methodology to create anisotropic high index nanoparticles. Although the ligand-metal force is effective in facilitating anisotropic growth, a major drawback is that such bimetallic crystals often lack strong internal interaction and structural coherence, easily decomposing or deactivating [9,33] when exposed to complex reaction environment [34].

Classic bottom up synthetic methodologies are primarily focused on ligand-mediated surface index for morphologically influenced catalysis (facet dependent catalysis), which can be attributed to activity enhancements of bimetallic nanocatalysts [35]. But recent research in nanomaterials has discovered that electron transfer and metal–metal interfacial strain can intrinsically enhance structural coherence and surface properties of bimetallic crystals [36–38], where extensive studies have shown that rather than forcing two metal species to form bimetallic nanoparticles using polymer stabilizers, lattice strain induced by difference in lattice parameters among the metal species can be used as a driving force to generate unique nanoparticles. Interfacial strain often induce unusual lattice stretch or contraction in bimetallic crystals. Such lattice distortion undoubtedly leads to tunable surface electronic properties and thus affecting catalytic activities of bimetals. This is because that the strong cohesive interaction at metal–metal interface (“ligand” effect) involves charge transfer or rehybridization of electron orbitals of two metals. The perturbation of a metal’s orbitals intrinsically shift *d* band towards/away from Fermi level [36]. Therefore, in the area of catalysis, this finding offers a new methodology and provides immense potential for innovative catalyst design [34,35]. Engineering optimal electronic coupling by altering metal–metal interfacial lattice strain and understanding its impact on catalytic activity of bimetallic materials have been attracting extensive attention in recent years [9,36,39].

There are three fundamental aspects which need to be addressed in present work: (a) proposing a ligand-free method for cooperative assembly of exchange coupled bimetallic nanocrystals, (b) investigating the plausible mechanism of lattice distorted and coupled growth of bimetallic crystals and (c) understanding how lattice distortion of crystals influences electronic coupling and surface catalytic properties. Using bimetallic PtMn crystal as a model system, we studied in this paper a polymer free one pot self-assembly method to synthesize exchange coupled nanoclusters. The anisotropic growth is induced by large lattice constant mismatch between the two metals (Pt: fcc, 0.39 nm; Mn: bcc, 0.89 nm). In this approach, well-controlled *bud-* and *cauliflower-shaped* PtMn clusters were grown in the absence of polymer stabilizers and immobilized on heterogeneous support (*i.e.* CeO₂) in one pot process. The influence of Pt/Mn ratio, solvent and chemical promoters on the lattice strain of PtMn clusters were systematically studied. Surface morphologies of PtMn catalyst samples were characterized using transmission electron microscopy (TEM), while information on Pt and Mn interaction, surface electronic properties and lattice distortion were obtained from X-ray photoelectron spectroscopy (XPS). A plausible mechanism for lattice distorted anisotropic growth of bimetallic PtMn is discussed. While reported studies on PtMn nanocatalysts deal with reactions involving simple substrates such as methanol [40–43], we investigated the performances of PtMn clusters for catalytic oxidation of renewable biomass-derived feedstocks (C_{2–3} polyols) in aqueous phase under relatively mild conditions (70 °C, 1 atm O₂).

This work shows that anisotropic growth induced lattice distortion and electronic coupling leads to exceptional (8 fold) enhancement in the activity of bimetallic PtMn nanocatalysts for oxidation of biomass feedstocks. The structure–activity correlation

of these catalysts obtained from biomass oxidation results provides guidance for rational design of synergistic bimetallic catalysts for selective activation of C–H and C–O bonds encountered in the processing of renewable fuels and chemicals.

2. Experimental section

2.1. Chemicals

Glycerol, lactic acid, glycolic acid, formic acid and dimethylformide (DMF) were purchased from Sigma Aldrich. Glyceric and tartronic acids were obtained from Fisher Scientific. Metal precursors such as Pt(acac)₂ and Mn(NO₃)₂ as well CeO₂ powders were also purchased from Sigma Aldrich.

2.2. Catalyst preparation

In a typical catalyst synthesis process, 1.2 g of CeO₂ powders and approximately 10 mL DMF solvent were first mixed at room temperature. Known amounts of Pt and Mn precursors were then charged and further mixed with the slurry till dissolved completely. Another 10 mL DMF was also added to the mixture. After transferring into a 100 mL autoclave, the whole slurry was flushed thrice with N₂ at room temperature. The whole mixture was heated at 200 °C under N₂ atmosphere (~2.2 MPa) for about 12 h before cooling down to room temperature. Catalyst powders from each batch of preparation were washed with ethanol/water (2/1 v/v) and centrifuged several times before drying under vacuum overnight. The catalyst samples were tested for oxidation without any further pre-treatment. The details of catalyst preparation method are described as follows:

Catalyst preparation was conducted *via* a simple solvothermal method. A schematic description of the preparation step is presented in Fig. 1. In particular, cerium oxide (CeO₂) supported Pt and PtMn catalysts were synthesized using DMF as a solvent. Unlike two-pot or seeded growth methods, reduction of metal precursors, Pt(acac)₂ and Mn(NO₃)₂·4H₂O, was performed in the presence of CeO₂ powder. In other words, both growth of nanocrystals and simultaneous immobilization on the catalyst support were achieved in one pot. The Pt content on CeO₂ support is 1 wt% for all the catalyst samples (identical Pt precursor concentration in all solution), while the atomic ratios of Pt/Mn (1/x) were varied from 1/0.5 to 1/2 (denoted as PtMn_x). In a typical catalyst preparation experiment, approximately 1.2 g catalysts were obtained in 20 mL DMF solution. While the CeO₂ powder and metal precursor solution in DMF are yellowish-white and brownish-yellow respectively, the solid products resulting from the one-pot synthesis are grey, suggesting reduction of metal precursors and immobilization of nanoparticles on the CeO₂ support. In addition, the gas atmosphere in the autoclave is also believed to be important in the formation and continuous growth of bimetallic nanocrystals. In most cases, N₂ was used as the inert blanket, while the reduction of metal precursors was induced by DMF (a weak reducing agent). In some control experiments, H₂ (a strong reducing agent) was added, while in another case benzoic acid (BA, a template agent) was used as a promoter in the DMF medium (see Table S1 for notation).

2.3. Oxidation tests

The experimental procedure for testing catalyst activity for glycerol oxidation was similar to that described previously [44]. Briefly, about 0.05 g of solid catalyst was added to 25 mL aqueous solution containing glycerol (1.0 g) and NaOH (1.7 g), which was transferred to a 100 mL of three neck flask. The slurry was heated in an oil bath with precise temperature control before heating up to a predetermined reaction temperature. Once the liquid slurry attained the

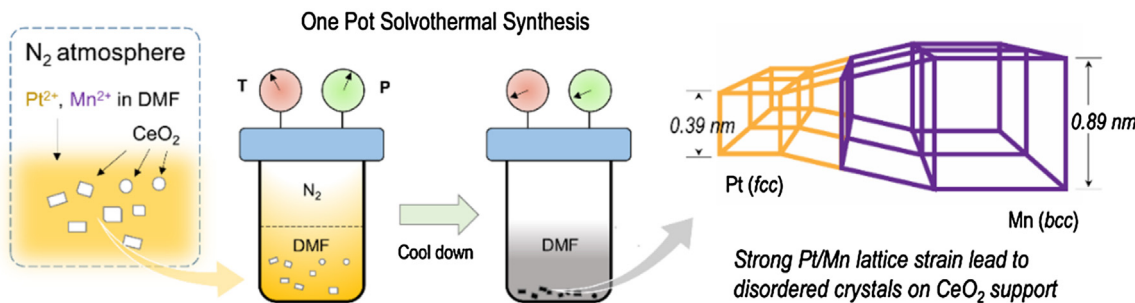


Fig. 1. Schematic description of one pot solvothermal synthesis of PtMn catalyst.

reaction temperature, stirring rate was set at 1000 RPM, and O₂ was introduced into the reactor at a constant rate (60 std mL/min), which signified the start of an experimental run. For recycle studies, catalyst samples were centrifuged to separate from reaction slurries and used for next run without any pretreatment.

2.4. Product analysis

Small amounts of liquid samples were withdrawn during batch studies and acidified with H₂SO₄ solution before injecting in HPLC (SHIMADZU with SH1011 column, see Fig. S3 for an example HPLC result). After each batch experiment, the volume of liquid mixture was measured to ensure negligible loss of solvent (<0.4 mL). From the concentration-time profiles, conversion (X), selectivity (S), carbon balance (C%) and turnover frequency (TOF based on surface Pt atoms, in h⁻¹) were calculated as defined below. Due to the complex structures of PtMn bimetallic nanocatalysts, it is difficult to distinguish surface Pt metal atoms from Mn. But TOF based on Pt dispersion was still used in this manuscript as an approximation to evaluate the performances of Pt and PtMn catalysts in oxidation reactions (Table S1) [45].

3. Results and discussion

3.1. Particle morphologies of Pt and PtMn nanoclusters

The TEM images of Pt, PtMn_{0.5}, PtMn₁, PtMn_{1.5} and PtMn₂ catalysts were first collected. Particle size and lattice spacing measurements were carried out in detail. It is seen from Figs. 2–4 that Pt and PtMn with increasing Mn content show different morphologies. As shown in Fig. 2(a, b), in the case of monometallic Pt/CeO₂ catalyst, 11.8 ± 3.8 nm sized Pt nanoparticles exhibit polyhedron shapes on the surface of CeO₂ support. The monometallic Pt catalyst without Mn doping displays ordered structures with (111) and (100) exposed as the dominant surface planes. When a small amount of Mn species was present, we observed that PtMn_{0.5} sample has slightly bigger particle size distribution in the range of 14.2 ± 3.5 nm with irregular shapes, as shown in Fig. 2(c). This difference suggests that the addition of Mn species interrupts the regular growth of Pt crystals during catalyst preparation and creates structures with defects. In particular, unlike monometallic Pt sample, it is found that PtMn_{0.5} nanoparticles are more irregularly shaped with clear formation of several heteroclusters. For example, most of the bimetallic PtMn_{0.5} particles in Fig. 2(c) inset display mixed shapes including branched and cubic particle features. There is evidence that some particles in this sample begin to form heteroclusters with twin structures within one particle. A detailed inspection of PtMn_{0.5} in Fig. 2(d) indicates that twinned structures with clearly different lattice spacing is present in several observed regions. This is possibly because the large lattice mismatch between Pt (0.39 nm) and Mn (0.89 nm) facilitates the anisotropic growth of bimetallic PtMn clusters forming heterogeneous rather than

regularly-shaped structures. As in the case of lattice mismatched PtFe heteroclusters, both anisotropic growth and galvanic displacement between Pt²⁺ and Fe as well as Pt and Fe³⁺ play critical roles in the formation of nanoclusters [46]. However, in the case of PtMn, it is strongly believed that lattice mismatch is the main driving force to influence anisotropic growth of PtMn clusters.

It is already established that kinetic rate of reduction of metal cations (e.g. Pt²⁺, Mn²⁺) can be controlled to tailor the morphology of the final particles [6,23]. Previous literature using NaBH₄ (strong reducing reagent) and electron deposition (reduction) have confirmed that fast reduction of metal cations results in predominantly small seeds/clusters with low surface indexed cubic and spherical shapes [25,42,47]. The DMF used in this study as a mild reducing agent can potentially generate different crystal structures. This hypothesis is confirmed when adding more Mn species in Pt system. As shown in Fig. 3(a–c), novel nano-bud shaped bimetallic clusters were formed in PtMn₁ sample. Each bud is approximately 5 nm wide and 23.8 ± 4.3 nm in diameter. Further inspection of selected PtMn₁ clusters show that most of them have four to eight buds [Fig. 3(d, e)]. The multiplicity of buds in each structure indicates anisotropic growth possibly orienting from the surface plane of ordered Pt octahedral or cubic structures, which has already been shown in the PtMn_{0.5} sample. In other words, it is plausible that when Mn is present in the Pt-based system, newly formed Pt species tend to deposit on mismatched Mn template and further grow in an epitaxial and anisotropic fashion [41]. This hypothesis is confirmed by the fact that between each bud within one particular cluster, clear disordered boundaries are present [Fig. 3(f)]. This information suggests that the lattice mismatch between Pt and Mn facilitates the formation of anisotropic and disordered layers wherein the buds can grow further. Thus, the heterogeneity of such materials may be further enhanced.

Clearly, the formation of bud-shaped PtMn₁ clusters results from internal lattice strain between Pt and Mn metals rather than being induced by template containing polymer ligands. Thus, the proposed novel methodology involving lattice-strain induced growth shows advantageous features over conventional methodologies, where ligands are often used to induce anisotropic growth of Pt-3d metals [4,5,17].

3.2. Lattice distortion and asymmetric structures

A close examination of selected domains in PtMn_{0.5} and PtMn₁ reveals the lattice distortion at the interface. Specifically, we measured lattice spacing in Fig. 2(f) and found that lattice spacing of Pt (100) facet has been stretched from approximately 0.19 nm (pure Pt (100)) to 0.23 nm. Such lattice stretching for Pt species obviously exists close to the boundaries of Pt and Mn lattices. Such unusual lattice distortion for PtMn crystals is possibly caused by DMF solvent annealing effect. Since it is known that DMF also act as ligand to mediate Pt (111) growth [16], it would be interesting to compare the significance of ligand and annealing effects during the

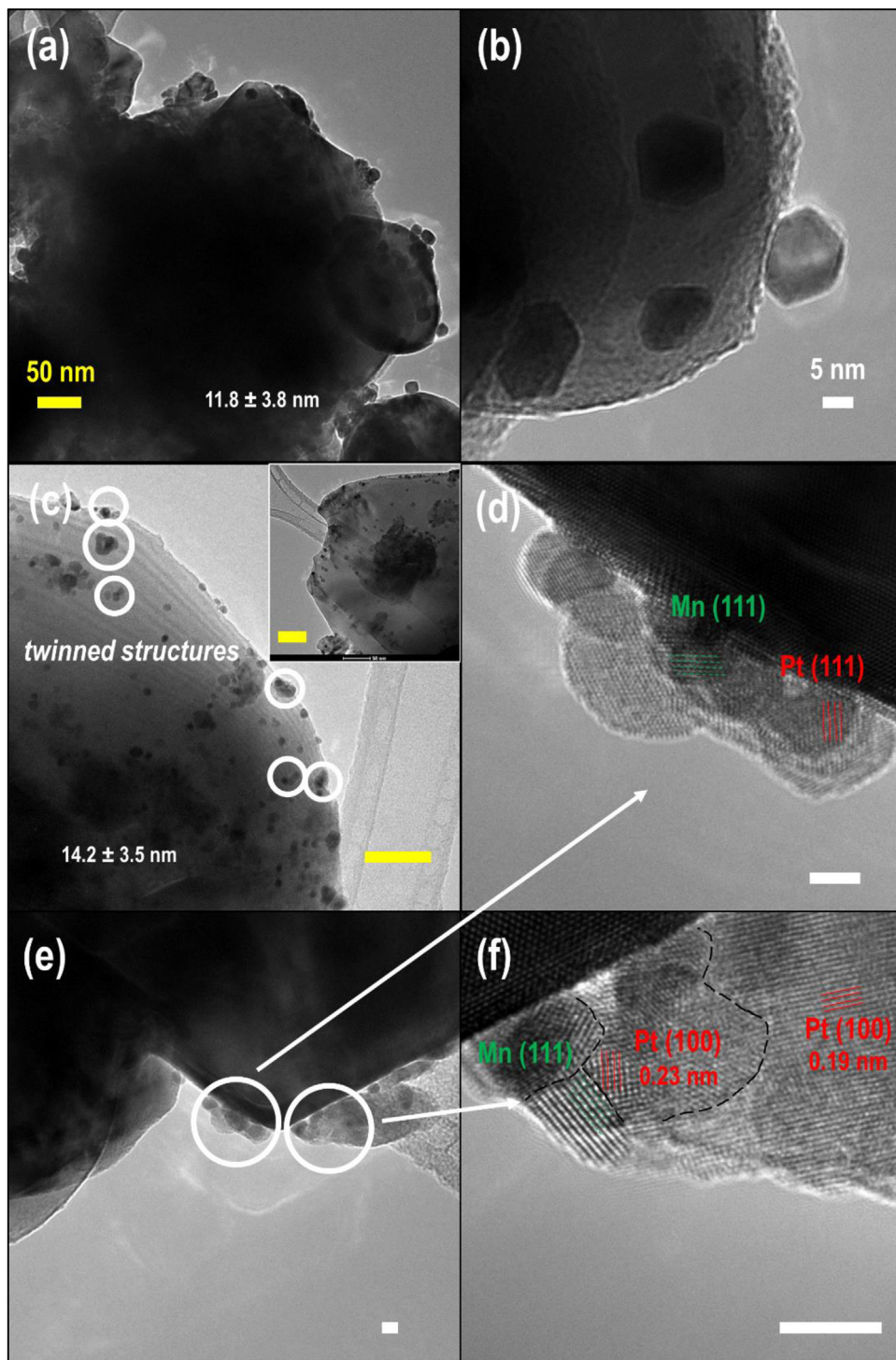


Fig. 2. TEM images of (a, b) monometallic Pt and (c–f) bimetallic $\text{PtMn}_{0.5}$ catalysts.

assembly of PtMn crystals. Therefore, detailed inspection of Fig. 2(f) was compared with that for Fig. 3(f). When more Mn species is present, Pt(100) surface has been minimized while Pt(111) is more predominant. Considering the morphological changes for PtMn_1 from $\text{PtMn}_{0.5}$, it is plausible that annealing and mediating influence of DMF solvent occur on Pt(111) surface.

The composition dependent morphology changes observed in this work motivated us to further understand how the presence of Mn species affects the size, shape and heterogeneity of PtMn clusters. Fig. 4 presents TEM images of PtMn samples with increased Mn

contents ($\text{PtMn}_{1.5}$, PtMn_2). As shown in Fig. 4(a), when Mn content increases from PtMn_1 to $\text{PtMn}_{1.5}$, some of the nano-buds appear to have merged into a flower shape. High resolution TEM (HR-TEM) images in Fig. 4(b, c) confirm that the length of each bud significantly increases from 5 nm to 10 nm for the $\text{PtMn}_{1.5}$ sample. While the lattice spacing of bud is consistent in PtMn_1 and $\text{PtMn}_{1.5}$ samples, HR-TEM images of the $\text{PtMn}_{1.5}$ catalyst sample shows that the particle size (flower size) is enhanced significantly to 35.9 ± 5.8 nm. Enhanced bud length does not show isotropic features but displays several mismatched layers within the structure of one bud. This

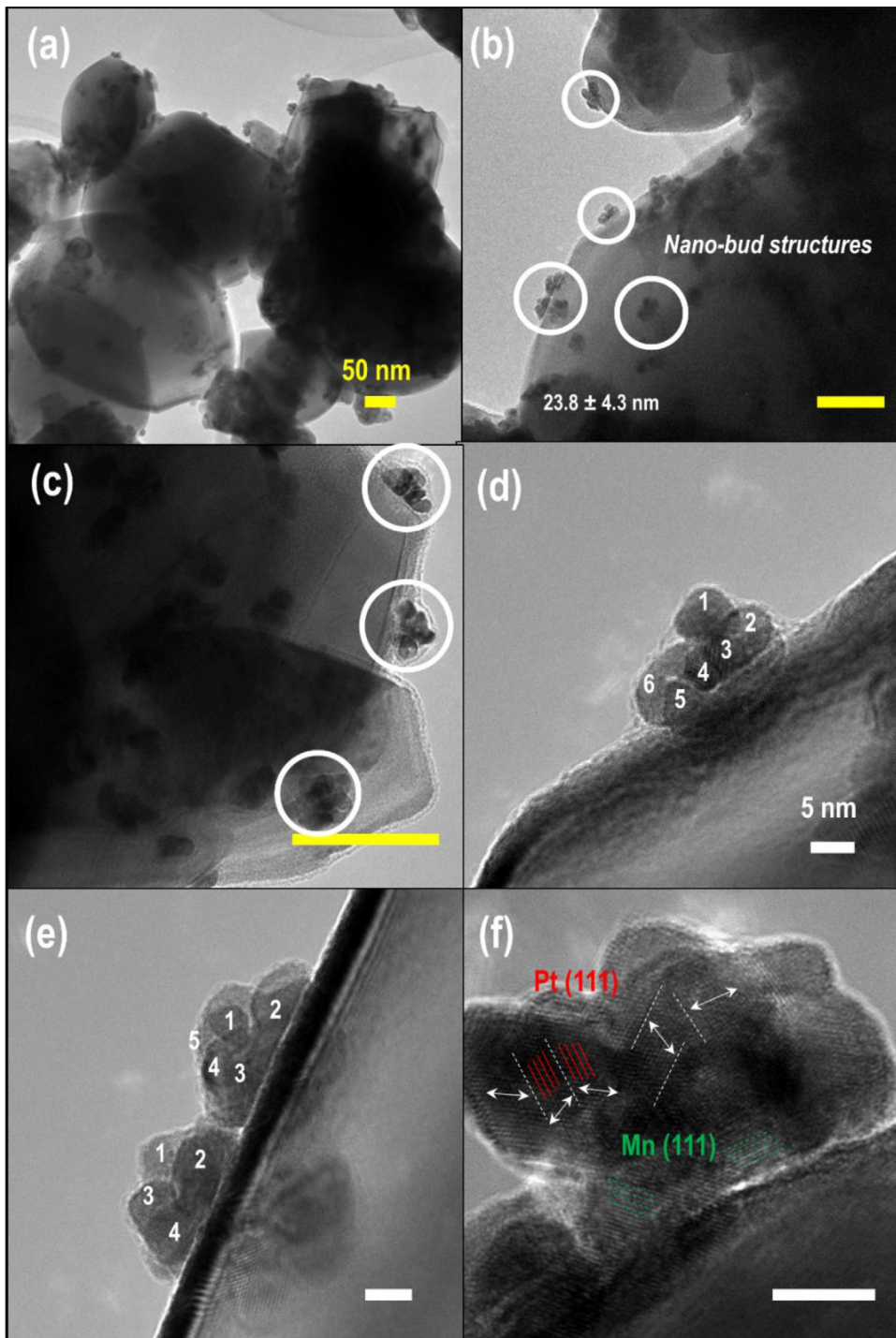


Fig. 3. TEM images of bimetallic PtMn₁ catalysts.

observation implies that Pt species, rather than forming additional nuclei on the support, tend to deposit on existing “bud templates” and facilitate size growth when more Mn species are present (*via* the Oswald mechanism). Thereby, the bud cluster evolves into a flower-shape cluster with increased dimensions. In the PtMn₂ sample [Fig. 4(d)], the average particle size of bimetallic clusters was enhanced to approximately 49 nm. This suggests that the increased Mn content in the Pt system facilitates the epitaxial growth of PtMn clusters rather than forming new Pt seeds, resulting in the formation of cauliflower-shaped structures with >15 buds in each cluster [Fig. 4(e)]. It is further found that as the length of the bud grows,

the gap between each bud shrinks significantly. Flower structures thus become very compact, which could reduce the overall surface area of nanoparticles exposed for catalytic reactions.

The TEM images for PtMn₁, PtMn_{1.5} and PtMn₂ samples also reveal the existence of several asymmetric structures [see Figs. 3(c-e) and 4(b, c, e, f)]. As mentioned previously, conventional methods usually involve the formation of nanoparticles or nanocluster from nuclei emanating in a homogeneous solution (oil or water phase). Symmetric structures typically result from these conventional approaches. In addition, the as prepared nanoclusters were washed and impregnated on solid supports (e.g. carbon)

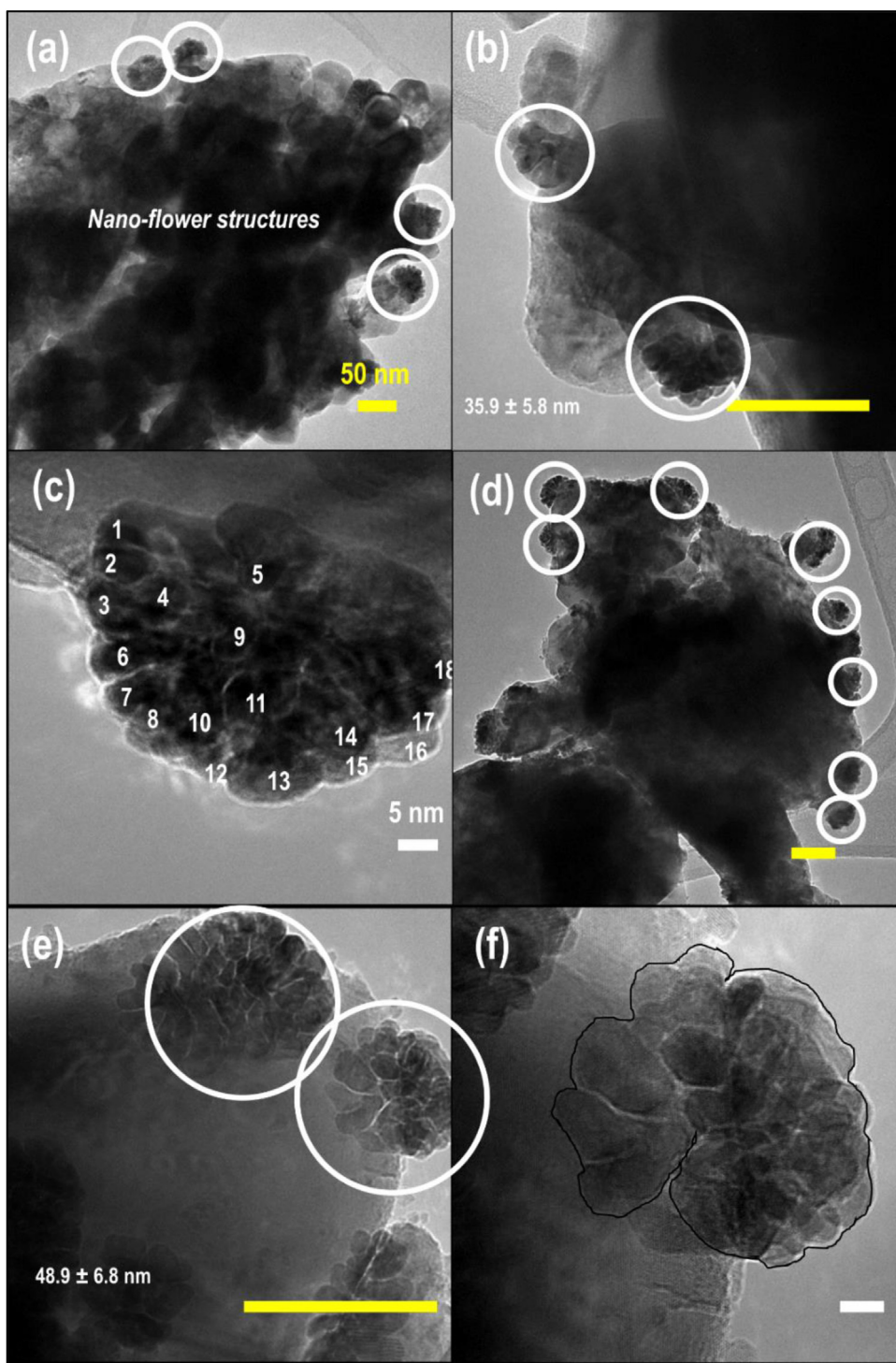


Fig. 4. TEM images of bimetallic (a–c) $\text{PtMn}_{1.5}$ and (d–f) PtMn_2 catalysts [boundaries in (f) was marked in black lines].

[6,48–50]. Therefore, the support does not play any role during cluster formation. In sharp contrast, in this study, we observed that the flower-shaped clusters actually grow and orient from solid support (*i.e.* CeO_2). In other words, the flower-shaped PtMn clusters tend to form at liquid-solid interface and further grow towards the liquid phase (source of metal precursors). While the influence of heterogeneous support on final particle morphologies could be a topic of another report, it is clear from this work that the presence of CeO_2 plays an important role in the formation of the observed bimetallic PtMn nanoclusters with novel features.

3.3. Factors influencing morphology of PtMn clusters

Based on the TEM characterization shown above, it is clear that the morphology of PtMn displays a strong dependence on Mn content. We also investigated the dependence of the growth of PtMn nano-buds on other experimental variables, such as the gas deployed (in the presence of H_2 instead of N_2) and chemical promoters/inhibitors (*e.g.*, BA) to gain mechanistic insights into cluster growth and also understand how chemical reagents affect the cluster morphologies.

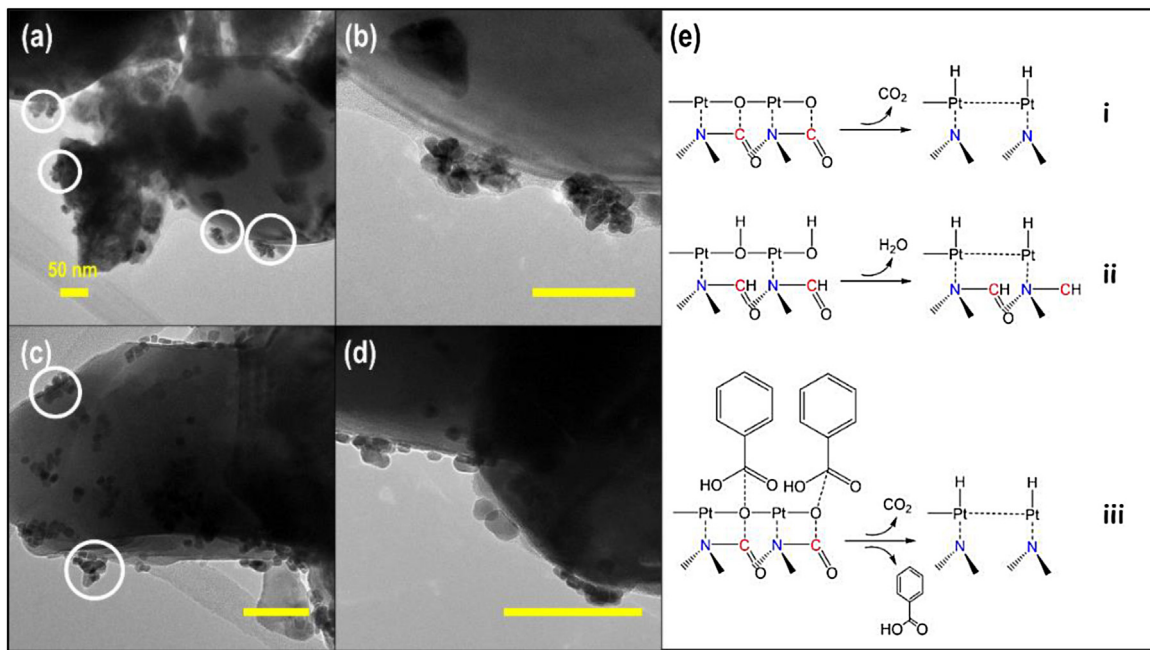


Fig. 5. TEM images of bimetallic (a and b) PtMn₁(H), (c and d) PtMn₁(BA) catalysts and (e) plausible reduction mechanism of metal ion reduction by (i) DMF, (ii) DMF + H₂ and (iii) DMF + BA.

3.3.1. H₂ atmosphere

PtMn₁(H) was prepared in a H₂ (rather than inert N₂) atmosphere under otherwise similar synthesis conditions used for the PtMn₁ sample. As shown in Fig. 5(a, b), rather than forming nano-bud structures, PtMn₁(H) sample tends to form much larger flowers, although the size of each bud is still small (approximately 6 nm). Clearly, the enhanced crystal size reduces the overall surface area of the PtMn₁(H) sample. The difference in morphology between PtMn₁ and PtMn₁(H) suggests that (a) the amine groups in DMF slowly reduce metal precursors in the liquid/solid slurry medium, (b) the growth kinetics are controlled by C=O groups in DMF [see (i) in Fig. 5(e)], and (c) H₂ tends to competitively interact with both metal precursors in the liquid phase and existing metallic species in the solid phase against the C=O groups. Thus enhanced reduction of metal cations to metallic clusters is facilitated, leading to facile anisotropic growth of the bimetallic PtMn clusters [51]. In other words, while C=O group interacts mildly with metal precursors, H₂ is a strong reducing agent that enhances the deposition rate of the metals, resulting in larger cluster sizes relative to the PtMn₁ sample prepared in N₂ atmosphere. This hypothesis appears to be inconsistent with previously reported findings because the bonding between C=O and metal is known to be very stable at low temperature [9,10,16]. Considering the slow reduction kinetics associated with DMF (weak reducing agent) compared to H₂ and solvothermal conditions (200 °C), it is concluded that the influence of C=O groups on the morphologies of PtMn₁(H) is negligible compared to the PtMn₁ sample. Such slow reduction kinetics in the presence of C=O is favorable for the formation of nano-bud structures [see (ii) in Fig. 5(e)].

3.3.2. Chemical promoter/inhibitor

The interesting observation with H₂ atmosphere led us to further explore how the nature of solvents, chemical promoters or inhibitors affects the growth of PtMn clusters. The TEM images in Fig. 5(c, d) are shown for the PtMn sample prepared by adding benzoic acid (BA) in DMF solvent [PtMn₁(BA)]. We find that the addition of benzoic acid (BA) corrodes the surface of CeO₂ support leading to formation of needle like structures (Fig. S2). More importantly, it is

found that a large number of particles tend to form string-shaped structures on the support surface rather than nano-bud shapes. In addition, isolated particles were also found within the PtMn₁(BA) sample. The differences among PtMn₁, PtMn₁(H) and PtMn₁(BA) suggest that carboxylic groups in benzoic acid molecules also play a role of weak template during cluster formation. However, the relatively large benzoic ring in BA structure possibly tends to sterically hinder the closed packing of nano-bud in the sample more significantly compared with amine group in DMF. The PtMn₁(BA) sample therefore does not display clear three dimensional cluster structures [see (iii) in Fig. 5(e)].

We also performed EDX mapping for selected bimetallic PtMn catalyst samples to understand how lattice mismatch and relative Pt/Mn content influence Pt and Mn dispersion. Fig. 6(a)–(d) present elemental mapping for PtMn_{0.5}, (b) PtMn₁, (c) PtMn₂ and (d) PtMn₁(H) catalyst samples, respectively. It is observed from Fig. 6(a) that Pt and Mn elements are not evenly distributed within selected nanoclusters. In other words, it is plausible that Pt and Mn species tend to deposit on different sites, which enables anisotropic growth of bimetallic PtMn clusters. Therefore, it is plausible that lattice mismatch force (strain) may prevent Pt and Mn from forming uniform alloy structures during reduction of metal precursors. When more Mn is present in PtMn system, the heterogeneity of clusters is further enhanced. From the TEM images (Figs. 3 and 4) and the element mapping, it appears that the strain generated from the lattice mismatch creates more interfacial boundaries that might be important for enhanced surface properties. This finding further confirms our hypothesis regarding anisotropic growth of PtMn clusters, resulting in defect induced structures. For increased Mn content in the PtMn system, it seems plausible that the particle growth and the agglomeration of Mn (*via* phase segregation) become more significant in comparison to lattice mismatch induced phase boundaries.

3.4. Plausible growth mechanism for PtMn clusters

Based on the parametric studies discussed in the previous section, a plausible mechanism for PtMn cluster formation and growth

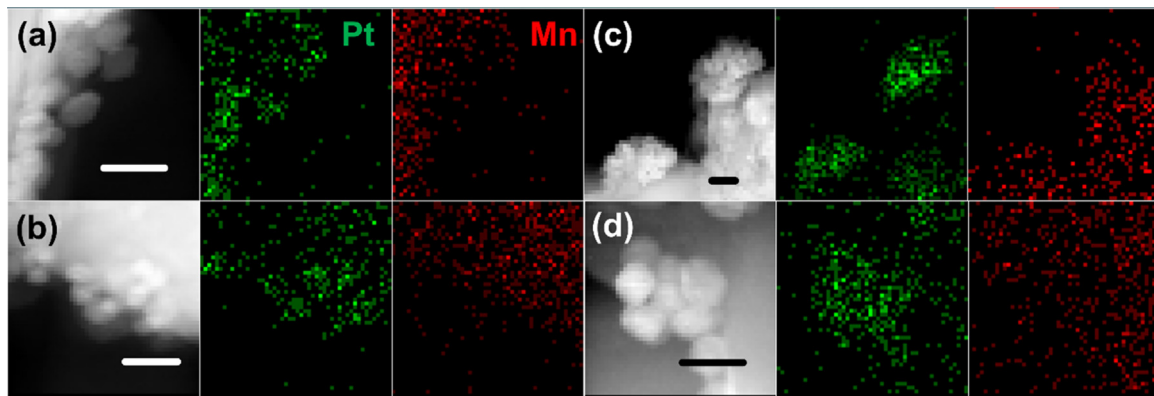


Fig. 6. EDX Mapping of (a) PtMn_{0.5}, (b) PtMn₁, (c) PtMn₂ and (d) PtMn₁(H) catalyst samples (white and black bars indicate 10 nm range).

is proposed. The nuclei for cluster formation is believed to occur as follows. Once Mn species is added to Pt system, the formation of Mn atoms on existing Pt crystals creates a strong surface tension due to large lattice mismatch between the two metals. A trace amount of Mn on Pt surface results in anisotropic growth of the Pt nuclei. In other words, the stacking faults break the surface orientation of Pt template and enables the formation of anisotropic structures [52]. Hence, it is plausible that PtMn twin structures, as opposed to Pt clusters, act as a template for the formation of nano-buds. While the formation of PtMn template occurs at a relatively fast rate, further growth of each bud might require relatively longer time even though they become thermodynamically favorable with the formation of new seeds in the liquid/solid medium [9,10,16].

The further growth of PtMn nano-bud into cauliflower shape is believed to occur as follows. If the isotropic growth of nano-bud is dominant, straight and uniform long bud structures should be expected when Mn loading is higher in PtMn system (e.g. PtMn₁, PtMn_{1.5}). However, from Figs. 4 and S1, it is found that most of the long buds (branches) consist of lattice mismatched layers. This observation suggests that the surface deposition of both Pt and Mn species during the reduction of metal precursor forms new atomic metal layers with a large quantity of defects. These flawed surface geometries may enhance the overall active sites for catalytic reactions. As the Mn content is further increased, the surface deposition becomes dominant while nucleation of seeds is almost negligible under solvothermal conditions. In addition, it is worth mentioning that Pt/Mn ratios also have direct impact on cluster sizes. It is clear in Fig. 3 that when Mn content is low, the average size of bimetallic PtMn particles is also small. But when more Mn is present in the system, we find that the size of bimetallic PtMn is enhanced significantly, which is also much larger than monometallic Pt particles. Based on existing theories of metallic atom deposition, we propose that the presence of Mn itself could act as a chemical promoter for crystal growth.

3.5. Catalytic oxidation of biomass-derived substrates to carboxylic acids

We studied how the novel PtMn cluster structures influence the catalytic oxidation of biomass-derived feedstocks. Specifically, oxidation of glycerol (GLY, a C₃ polyol), 1,2-propanediol (PDO, a C₃ polyol), ethanol (EtOH, a C₂ alcohol) and ethylene glycol (EG, a C₂ polyol) were investigated on selected PtMn catalysts to understand the oxidation activity trends for polyols and alcohols. Catalytic oxidation reactions were carried out under very mild conditions (70 °C, 1 atm O₂) with carboxylic acids being the target products.

Using the methodology described elsewhere [46], we estimated that gas-liquid (for O₂ molecule), liquid-solid and intraparticle (O₂

and substrate) mass transfer limitations are insignificant compared to the observed reaction rates. The activity for each investigated catalyst was calculated based on the intrinsic kinetic rate at low conversion levels (~23%) and the measured Pt metal dispersion, the details of which are presented in Table S1.

The influence of cluster size on the activity of the PtMn nanocatalysts for GLY oxidation is shown in Fig. 7(a). We observed a peak activity value of 17,836.9 h⁻¹ on PtMn₁ (Pt/Mn: 1/1 molar ratio) clusters, dropping significantly for PtMn_{1.5} (9911 h⁻¹) and PtMn₂ (3231 h⁻¹) catalysts. Concentration-time profiles of GLY oxidation over PtMn₁ catalyst [Fig. 7(b)] show that GLY concentration dropped from 0.43 kmol/m³ to zero within 6 h with glyceric acid (GLYA), the primary GLY oxidation product, being the dominant one. Interestingly, the GLYA concentration decreases gradually with increasing concentration of tartronic acid (TAR), glycolic acid and oxalic acid, implying that secondary oxidation (GLYA to TAR) and C–C cleavage occur after GLY was consumed. The PtMn₁ catalyst outperforms most investigated nanocatalysts reported in the literature (see Table S2 in supporting information). Although the activity of PtMn₁ catalyst is slightly lower than the recently reported activity for bimetallic PtFe catalysts (TOF: 20,978 h⁻¹), the selectivity towards TAR (53% on PtMn₁), a valuable dicarboxylic acid product, is higher than observed on PtFe catalysts (42%).

As already shown in Fig. 5, the addition of H₂ and BA has been found to influence the morphology of the bimetallic PtMn clusters. While the observed activity of PtMn₁(H) and PtMn₁(BA) catalysts is less than the activity of PtMn₁ catalyst, they also exhibit enhanced TOFs [see Fig. 7(c) and Table S1 for details] compared to the monometallic Pt catalyst. The observed oxidation activity for other bio-derived alcohols and polyols such as EG and EtOH reveal that as the carbon number decreases from 3 to 2, the reactivity of polyols decreases. Furthermore, we also observed that reactivity of GLY and EG is higher than that of PDO and EtOH. This difference implies that substrates with more electron withdrawing groups (higher oxygen content) exhibit relatively higher reactivity during aqueous phase oxidation reactions.

Recycle tests were also carried out to study the durability of PtMn₁ catalyst during oxidation of GLY. Results in Table 1 show good stability of PtMn₁ catalyst in terms of activity and selectivity. It is also found that the total metal leaching for Pt and Mn after two recycles is 0.50% and 3.3%, indicating good stability of PtMn₁ catalyst under reaction conditions.

3.6. Lattice distortion induced reconfiguration of electrons

The results obtained from the experimental conversion studies, in conjunction with TEM characterization on bimetallic nanocrystals, provide fundamental insights into how lattice distortion

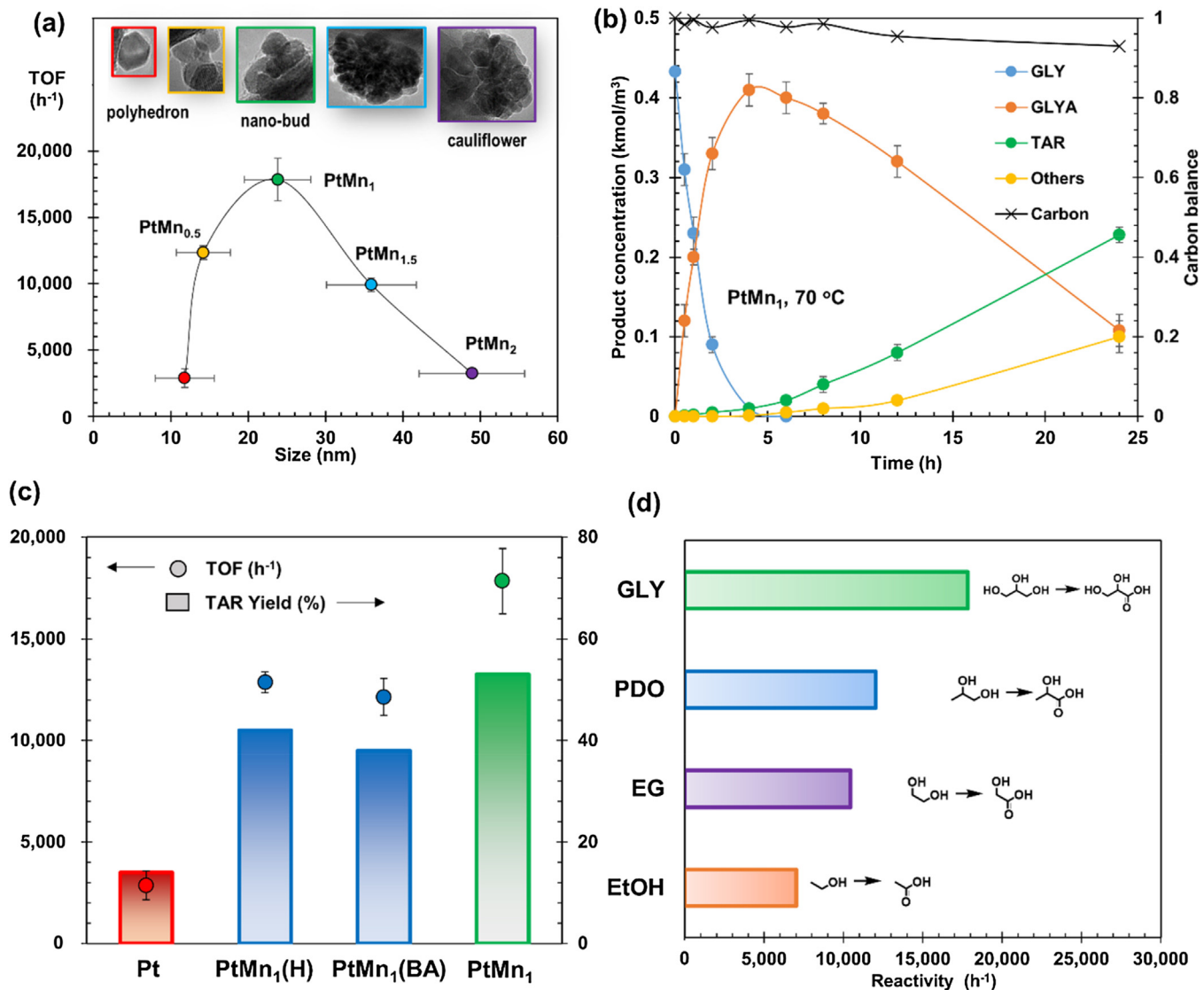


Fig. 7. Catalytic performances of PtMn catalysts for GLY oxidation. (a) composition-dependent activity, (b) a concentration-time profile in the presence of PtMn₁ catalyst at 70 °C and 0.1 MPa O₂, (c) catalytic performance comparison of mono Pt and bimetallic PtMn₁(H), PtMn₁(BA) and PtMn₁ (TAR yield obtained after 24 h reaction time), (d) oxidation of other bio-derived alcohols in the presence of PtMn₁ catalyst.

Table 1

Recycle tests of PtMn₁ catalyst for GLY oxidation at 70 °C.

PtMn ₁ catalyst	TOF (h^{-1})	Selectivity after 24 h reaction (%)			Metal leaching (%)
		GLYA	TAR	Others	
Fresh	17836.9	24.9	52.7	20.1	Pt: 0.5%
1st recycle	18100.1	22.1	55.8	18.1	Mn: 3.3%
2nd recycle	16966.7	26.4	51.2	19.9	

Refer "Experimental Section" for other experimental conditions. 100% conversion were obtained for all tests.

influences surface morphologies and thereby catalytic performance during aqueous phase oxidation over supported bimetallic nanoclusters. The mechanism of how lattice strain leads to electron reconstruction and synergistic enhancement in catalytic performance is yet to be fully understood. Therefore, several bimetallic PtMn catalyst samples were characterized using XPS to reveal the surface metal valence state, metal–metal coupling effect and possible reconfiguration of surface electrons. It is important to mention that each sample was repeatedly scanned to ensure reproducibility of XPS spectra. In Fig. 8, XPS spectra of Pt, PtMn_{0.5}, PtMn₁ and PtMn_{1.5} catalyst samples are presented in (a, b), (c–e), (f–h) and

(i–k), respectively. In particular, spectra in Fig. 8(a) and (b) were obtained for monometallic Pt catalysts and used as reference for bimetallic PtMn catalysts. Fig. 8(a) shows two characteristic peaks for Pt4f_{5/2} and Pt4f_{7/2} at 71–75 eV of binding energy, while Ce3d_{5/2} spectra at 883 eV and 892 eV are shown in Fig. 8(b). In addition, it is found from all bimetallic catalyst samples that Pt element exists in metallic form while Mn in oxide (MnO) form [53,54]. In bimetallic PtMn samples, as more Mn species were doped into Pt system, the binding energy for Pt4f_{5/2} and Pt4f_{7/2} began to shift. Specifically, the separated spin-orbits Pt4f_{5/2} and Pt4f_{7/2} exhibit shift towards lower binding energy in PtMn_{0.5} sample [see Fig. 8(c)]. This shift

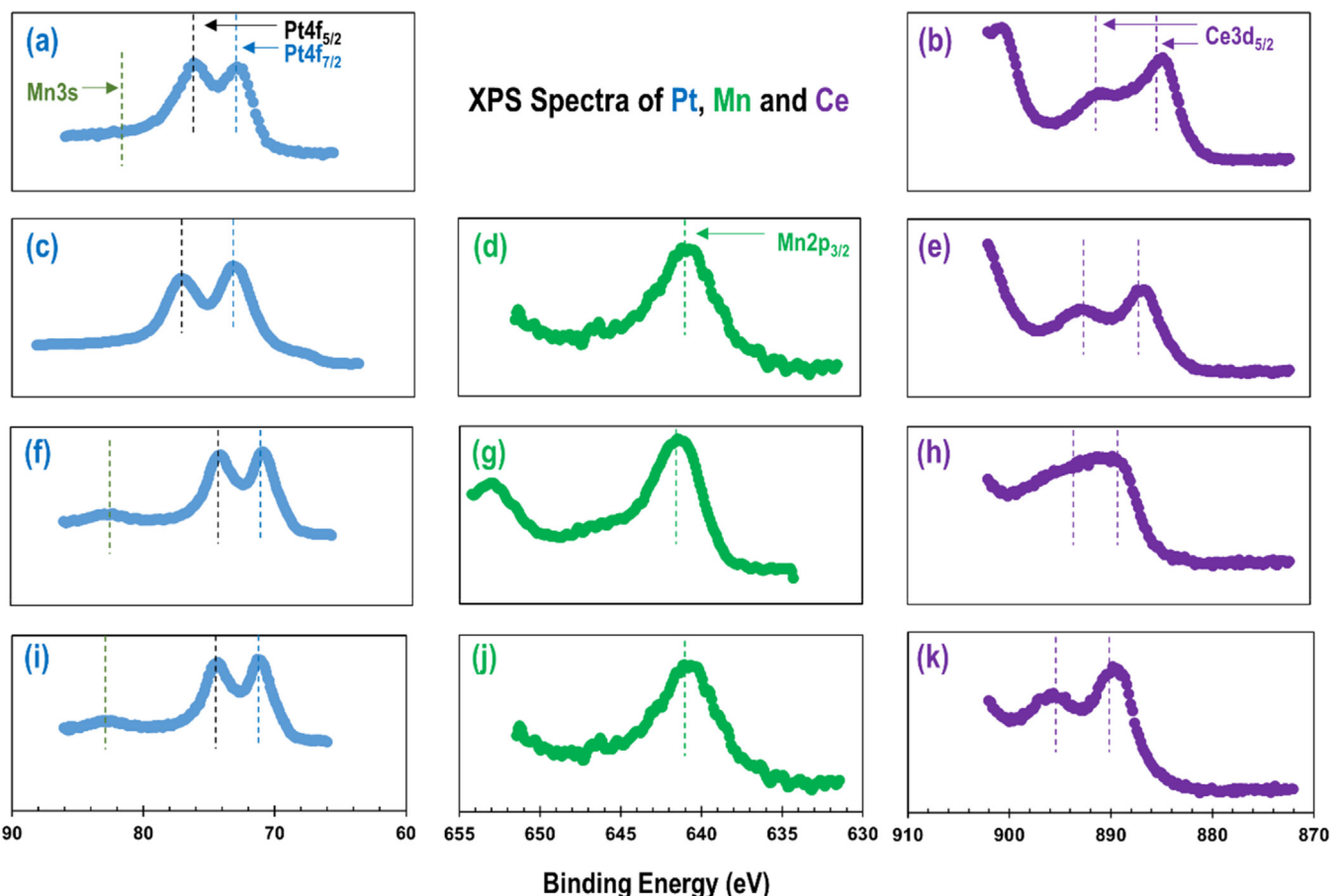


Fig. 8. XPS spectra of (a, b) Pt, (c–e) PtMn_{0.5}, (f–h) PtMn₁, (i–k) PtMn_{1.5} catalyst samples (XPS spectra for Pt, Mn and Ce in blue, green and purple respectively). (For interpretation of the references to colour in this figure legend, the reader is referred to the web version of this article.)

becomes gradually more significant for PtMn₁ [Fig. 8(f–h)] and PtMn_{1.5} [Fig. 8(i–k)] samples. In contrast, we observed that Mn2p_{3/2} exhibits a slight shift to higher binding energy. Obviously the lattice mismatch creates internal strain, leading to changes in binding energies for Pt and Mn species.

Changed local environment on metal surface atoms indicates that there might display an electronic coupling effect for Pt and Mn atoms. The lattice distance for Pt cells was stretched while that for Mn was contracted [39]. The changed lattice parameters modify Pt–Mn bond length and induce formation of strained layers within bimetallic crystals (as schematically described in Fig. 1). Such changes obviously alter the electronic structures of the two metals by orbital overlap and electronic coupling [36]. Although, a detailed mechanism is still unclear, the interaction between the two types of species obviously results in higher electron density on the Pt surface. This provides a plausible explanation for the enhanced oxidation activity observed with bimetallic catalysts. Quantitative XPS data showing that surface Pt/Mn atomic ratios are also dependent on bulk compositions, have been added to Table S3. Clearly, such changes in the surface properties may influence surface catalytic activity and selectivity. Based on XPS characterization, it appears that the interaction between Pt and Mn might be the key for synergistic catalytic activity in aqueous phase oxidation.

Based on the foregoing discussion, we propose the following surface reaction mechanism, a schematic description of which is shown in Fig. 9:

- (1) Monometallic Pt or bimetallic PtMn nanocrystals can be activated by molecular O₂ on the surface. In monometallic Pt

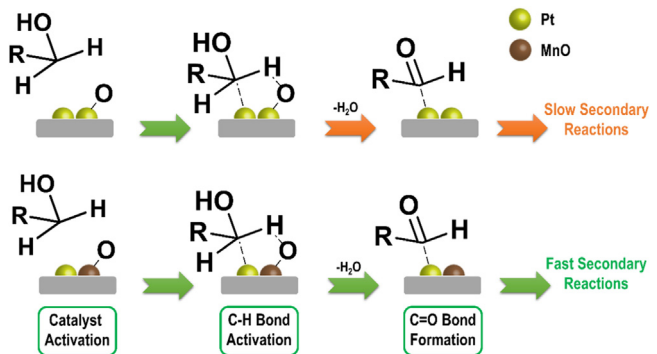


Fig. 9. Schematic description of possible surface reaction mechanism.

catalyst, Pt sites tend to attack side C atoms in polyol molecules [55], while adjacent O activated Pt sites tend to interact with the C–H bond [56]. On the other hand, on bimetallic PtMn catalyst surface, MnO is more easy to be activated due to relatively higher oxidation potential than Pt [57]. This is because compressed Mn lattices leads to a broadened d-band along the direction of strain (distortion) [39]. Theoretical predictions find that adsorption of atomic oxygen on MnO surface could be a key step for catalytically breaking O–H bond [58] by forming an intermediate ring on catalyst surface with adjacent Pt atoms [59]. Higher surface electron density on Pt metal surface is believed to facilitate activation of C–O bond [60] to form C=O bond.

- (2) Compared with monometallic Pt catalyst, bimetallic PtMn nanocrystals may have slightly lower binding energy of $-C=O$ groups [35], thus secondary reactions such as aldehydes to monocarboxylic acids as well as monocarboxylic to dicarboxylic acids can occur more easily on bimetallic surface. The presence of Mn species has clearly improved activity and selectivity of Pt catalysts. When no Mn is present, the strong interaction between $-C=O$ group and Pt inhibit secondary oxidation reactions but promoting side reactions [low selectivity to tartronic acid on monometallic Pt catalyst, Fig. 7(c)]. However, the interaction is weakened due to the addition of Mn content, which is evident by enhanced secondary oxidation reaction and higher tartronic acid selectivity [Fig. 7(b)]. Therefore, we conclude that lower binding energy is a dominant factor for enhanced selectivity towards tartronic acid, while stretched Pt lattice main contribute to enhanced catalytic activity (higher d-band center energy) [21,40,43]. Oxidation reactions consume surface oxygen species thus catalytic sites can be available for subsequent cycles.
- (3) Interestingly, the overall reactivity of PDO and EtOH is lower than GLY and EG. This suggests that the R groups in these substrate molecules also affect their overall reactivity. Methyl (CH_3-) is an electron donating group and the existence of such a group in the substrate molecules increases the electron density of reactive C, therefore unfavorably preventing attack by Pt sites during catalytic reactions. This mechanism is validated by XPS characterization of Pt and PtMn catalysts, their catalytic performances, and reactivity trends of polyols. Therefore, it is clear that the addition of Mn in Pt system alters the lattice parameters, resulting in electronic coupling and surface electronic thus synergistically enhancing the catalytic properties.

4. Conclusions

In this paper, we report a unique approach for the synthesis of novel structured PtMn nanocatalysts using lattice strain technique, which have exceptionally high catalytic activity in oxidation of polyols and alcohols. The formation of nuclei, growth of nanoclusters and immobilization on heterogeneous support were achieved in a one pot wet chemistry method. The influences of Pt/Mn ratios, synthesis conditions and chemical promoters on surface morphologies and catalytic properties of bimetallic PtMn were studied systematically. It is found that the large lattice mismatch between Pt and Mn metals leads to anisotropic growth while lattice distortion of bimetallic crystals is believed to be the key for synergistic enhancement of catalytic activity and selectivity. Aqueous phase oxidation of biomass-derived polyols was used as the model reaction to reveal the correlation of crystal morphologies with catalytic properties of bimetallic catalysts. The methodology for catalyst synthesis proposed in this work provides a new technique for designing active and selective nanomaterials for biomass as well as other renewable energy applications.

Acknowledgement

This work was partially supported by NSF/EPA grant CHE-1339661.

Appendix A. Supplementary data

Supplementary data associated with this article can be found, in the online version, at <http://dx.doi.org/10.1016/j.apcata.2017.01.021>.

References

- [1] X. Jin, L.N. Dang, J. Lohrman, B. Subramaniam, S.Q. Ren, R.V. Chaudhari, *ACS Nano* 7 (2) (2013) 1309.
- [2] W.J. Yan, A. Ramanathan, M. Ghanta, B. Subramaniam, *Catal. Sci. Technol.* 4 (12) (2014) 4433.
- [3] W.J. Yan, A. Ramanathan, P.D. Patel, S.K. Maiti, B.B. Laird, W.H. Thompson, B. Subramaniam, *J. Catal.* 336 (2016) 75.
- [4] X.M. Lu, M. Ryengen, S.E. Skrabalak, B. Wiley, Y.N. Xia, *Annu. Rev. Phys. Chem.* 60 (2009) 167.
- [5] R.G. Chaudhuri, S. Paria, *Chem. Rev.* 112 (4) (2012) 2373.
- [6] H.H. Li, C.H. Cui, S. Zhao, H.B. Yao, M.R. Gao, F.J. Fan, S.H. Yu, *Adv. Energy Mater.* 2 (10) (2012) 1182.
- [7] Y.J. Xiong, J.Y. Chen, B. Wiley, Y.N. Xia, S. Aloni, Y.D. Yin, *J. Am. Chem. Soc.* 127 (20) (2005) 7332.
- [8] G.Q. Ren, Y.C. Xing, *Nanotechnology* 20 (46) (2009).
- [9] Z.W. Quan, Y.X. Wang, J.Y. Fang, *Acc. Chem. Res.* 46 (2) (2013) 191.
- [10] N.S. Porter, H. Wu, Z.W. Quan, J.Y. Fang, *Acc. Chem. Res.* 46 (8) (2013) 1867.
- [11] B. Geboes, I. Mintsonouli, B. Wouters, J. Georgieva, A. Kakaroglu, S. Sotiropoulos, E. Valova, S. Armyanov, A. Hubin, T. Breugelmans, *Appl. Catal. B—Environ.* 150 (2014) 249.
- [12] I. Mintsonouli, J. Georgieva, S. Armyanov, E. Valova, G. Avdeev, A. Hubin, O. Steenhaut, J. Dille, D. Tsiplakides, S. Balomenou, et al., *Appl. Catal. B—Environ.* 136 (2013) 160.
- [13] B.I. Podlovchenko, V.A. Krivchenko, Y.M. Maksimov, T.D. Gladysheva, L.V. Yashina, S.A. Evlashin, A.A. Pilevsky, *Electrochim. Acta* 76 (2012) 137.
- [14] A. Sarkar, A. Manthiram, *J. Phys. Chem. C* 114 (10) (2010) 4725.
- [15] B.I. Podlovchenko, T.D. Gladysheva, A.Y. Filatov, L.V. Yashina, *Russ. J. Electrochim.* 48 (2) (2012) 173.
- [16] J.P. Lai, W.X. Niu, R. Luque, G.B. Xu, *Nano Today* 10 (2) (2015) 240.
- [17] J. Gu, Y.W. Zhang, F. Tao, *Chem. Soc. Rev.* 41 (24) (2012) 8050.
- [18] M. Wang, W.M. Zhang, J.Z. Wang, A. Minett, V. Lo, H.K. Liu, J. Chen, *J. Mater. Chem. A* 1 (7) (2013) 2391.
- [19] D.H. Chen, Y.C. Zhao, X.L. Peng, X. Wang, W.J. Hu, C. Jing, S.S. Tian, J.N. Tian, *Electrochim. Acta* 177 (2015) 86.
- [20] C. Gumeci, D.U. Cearnaigh, D.J. Casadonte, C. Korzeniewski, *J. Mater. Chem. A* 1 (6) (2013) 2322.
- [21] J.P. Lai, R. Luque, G.B. Xu, *ChemCatChem* 7 (20) (2015) 3206.
- [22] F. Nosheen, Z.C. Zhang, J. Zhuang, X. Wang, *Nanoscale* 5 (9) (2013) 3660.
- [23] R. Sakamoto, K. Omichi, T. Furuta, M. Ichikawa, *J. Power Sources* 269 (2014) 117.
- [24] K.A. Kuttiyiel, K. Sasaki, Y.M. Choi, D. Su, P. Liu, R.R. Adzic, *Nano Lett.* 12 (12) (2012) 6266.
- [25] W.Y. Wang, D.S. Wang, X.W. Liu, Q. Peng, Y.D. Li, *Chem. Commun.* 49 (28) (2013) 2903.
- [26] H. Zhang, D.R. Lin, G.T. Xu, J.B. Zheng, N.W. Zhang, Y.H. Li, B.H. Chen, *Int. J. Hydrogen Energy* 40 (4) (2015) 1742.
- [27] Z.R. Dai, S.H. Sun, Z.L. Wang, *Nano Lett.* 1 (8) (2001) 443.
- [28] J.Y. Li, G.X. Wang, J. Wang, S. Miao, M.M. Wei, F. Yang, L. Yu, X.H. Bao, *Nano Res.* 7 (10) (2014) 1519.
- [29] J. Yao, Y.F. Yao, *Renew. Energy* 81 (2015) 182.
- [30] L. Chen, C. Bock, P.H.J. Mercier, B.R. MacDougall, *Electrochim. Acta* 77 (2012) 212.
- [31] V.R. Stamenkovic, B.S. Mun, M. Arenz, K.J.J. Mayrhofer, C.A. Lucas, G.F. Wang, P.N. Ross, N.M. Markovic, *Nat. Mater.* 6 (3) (2007) 241.
- [32] N. Wakabayashi, M. Takeichi, H. Uchida, M. Watanabe, *J. Phys. Chem. B* 109 (12) (2005) 5836.
- [33] J.E. Mondloch, E. Bayram, R.G. Finke, *J. Mol. Catal. A: Chem.* 355 (2012) 1.
- [34] H. Liao, A. Fisher, Z.J. Xu, *Small* 11 (27) (2015) 3221.
- [35] A. Holewinski, H. Xin, E. Nikolla, S. Linic, *Curr. Opin. Chem. Eng.* 2 (3) (2013) 312.
- [36] E. Gross, G.A. Somorjai, *Top. Catal.* 56 (12) (2013) 1049.
- [37] J.B. Wu, P.P. Li, Y.T. Pan, S. Warren, X. Yin, H. Yang, *Chem. Soc. Rev.* 41 (24) (2012) 8066.
- [38] A. Kirkinde, S. Ren, *Nano Lett.* 14 (8) (2014) 4493.
- [39] J. Wu, P. Li, Y.-T.F. Pan, S. Warren, X. Yin, H. Yang, *Chem. Soc. Rev.* 41 (24) (2012) 8066.
- [40] C.W. Xu, Y.Z. Su, L.L. Tan, Z.L. Liu, J.H. Zhang, S.A. Chen, S.P. Jiang, *Electrochim. Acta* 54 (26) (2009) 6322.
- [41] Y.J. Kang, C.B. Murray, *J. Am. Chem. Soc.* 132 (22) (2010) 7568.
- [42] M. Ammam, E.B. Easton, *J. Power Sources* 236 (2013) 311.
- [43] M. Ammam, E.B. Easton, *J. Electrochim. Soc.* 160 (2) (2013) F212.
- [44] X. Jin, M. Zhao, J. Shen, W.J. Yan, L.M. He, P.S. Thapa, S.Q. Ren, B. Subramaniam, R.V. Chaudhari, *J. Catal.* 330 (2015) 323.
- [45] S.T. Oyama, X.M. Zhang, J.Q. Lu, Y.F. Gu, T. Fujitani, *J. Catal.* 257 (1) (2008) 1.
- [46] X. Jin, M. Zhao, W. Yan, C. Zeng, P. Bobba, P.S. Thapa, B. Subramaniam, R.V. Chaudhari, *J. Catal.* 337 (2016) 272.
- [47] K. Ono, R. Okuda, Y. Ishii, S. Kamimura, M. Oshima, *J. Phys. Chem. B* 107 (9) (2003) 1941.
- [48] S.H. Sun, C.B. Murray, D. Weller, L. Folks, A. Moser, *Science* 287 (5460) (2000) 1989.
- [49] H.M. Song, W.S. Kim, Y.B. Lee, J.H. Hong, H.G. Lee, N.H. Hur, *J. Mater. Chem.* 19 (22) (2009) 3677.
- [50] L. Gan, C.H. Cui, M. Heggen, F. Dionigi, S. Rudi, P. Strasser, *Science* 346 (6216) (2014) 1502.

- [51] C.H. Cui, L. Gan, H.H. Li, S.H. Yu, M. Heggen, P. Strasser, *Nano Lett.* 12 (11) (2012) 5885.
- [52] H. You, S. Yang, B. Ding, H. Yang, *Chem. Soc. Rev.* 42 (7) (2013) 2880.
- [53] M.S. El-Deab, T. Ohsaka, *Angew. Chem. Int. Ed.* 45 (36) (2006) 5963.
- [54] A.E. Vilian, M. Rajkumar, S.-M. Chen, C.-C. Hu, K.M. Boopathi, C.-W. Chu, *RSC Adv.* 4 (78) (2014) 41387.
- [55] B. Liu, J. Greeley, *J. Phys. Chem. C* 115 (40) (2011) 19702.
- [56] M. Salciccioli, W.T. Yu, M.A. Barreau, J.G.G. Chen, D.G. Vlachos, *J. Am. Chem. Soc.* 133 (20) (2011) 7996.
- [57] G.F. Nordberg, B.A. Fowler, M. Nordberg, *Handbook on the Toxicology of Metals*, Academic Press, 2014.
- [58] H.-Y. Su, Y. Gorlin, I.C. Man, F. Calle-Vallejo, J.K. Nørskov, T.F. Jaramillo, J. Rossmeisl, *Phys. Chem. Chem. Phys.* 14 (40) (2012) 14010.
- [59] J. Trawczyński, B. Bielak, W. Miśta, *Appl. Catal. B: Environ.* 55 (4) (2005) 277.
- [60] M.U. Khan, L. Wang, Z. Liu, Z. Gao, S. Wang, H. Li, W. Zhang, M. Wang, Z. Wang, C. Ma, *Angew. Chem.* (2016).